PERGAMON

International Journal of Heat and Mass Transfer 42 (1999) 873–887

International Journal of HEAT and MASS TRANSFER

Mass transfer in turbulent impinging slot jets

Qian Chen, Vijay Modi*

Department of Mechanical Engineering, 500 West 120th Street, Mail Code 4703, Columbia University, New York, NY 10027, U.S.A.

Received 27 January 1998; in final form 15 June 1998

Abstract

The mass transfer characteristics of a turbulent slot jet impinging normally on a target wall are examined using numerical simulations. At the location where the slot jet emerges from the nozzle, a confinement plate is placed parallel to the target plate. The jet fluid is the same as the otherwise stagnant fluid into which the jet emerges. Fluid flow is modeled using the k–ω turbulence model of Wilcox [1]. The computations are validated against existing experimental fluid flow, heat transfer and mass transfer data. The range of Reynolds numbers examined is from 450 to 20 000 with Prandtl or Schmidt numbers from 1 to 2400. The distance of the target plate from the slot jet varies between 2 and 8 times the slot jet width. The study reveals computational aspects that are unique to the solution of flow and mass transfer problems with the combination of high Schmidt numbers and turbulent flows.

Nomenclature

B slot jet width [m]
c concentration of chemical species [kg mol^{-1} m^{-3}]
C_f skin friction at the impingement plate, $C_f = \tau_w/\frac{1}{2}\rho v_{in}^2$
D diffusion coefficient [m^2 s^{-1}]
G production rate of turbulence kinetic energy [m^2 s^{-3}]
H distance from slot jet to the impingement wall [m]
I inlet turbulence intensity, $I = \sqrt{((u'^2+v'^2+w'^2)/3)}/(v_{in})$
k turbulence kinetic energy [m^2 s^{-2}]
L computational domain length [m]
Nu Nusselt number
p pressure [N m^{-2}]
Pr Prandtl number
Re Reynolds number, defined as $Re = v_{in}B/v$
R_k closure coefficient $R_k = 6$
R_t^* turbulent Reynolds number, defined as $R_t^* = k/\omega v$
R_w closure coefficient, $R_w = 2.7$
R_β closure coefficient, $R_\beta = 8$
Sc Schmidt number
Sh Sherwood number
s_i surface area of the control volume face in i direction [m^2]
t time [s]
u mean velocity in x direction [m s^{-1}]
u_i mean velocity [m/s]
u_i' fluctuating component of velocity [m s^{-1}]
v mean velocity in y direction [m s^{-1}]
v_{in} average velocity of slot jet [m s^{-1}]
x coordinate direction parallel to impingement plate [m]
x_i x ($i = 1$) and y ($i = 2$) coordinates [m]
y coordinate direction normal to impingement plate [m].

Greek symbols

α damping function defined as $\alpha = \frac{5}{9}(\hat{\alpha}+R_t^*/R_w)/(1+R_t^*/R_w)(\alpha^*)^{-1}$
$\hat{\alpha}$ closure coefficient, $\hat{\alpha} = 1/10$
$\hat{\alpha}^*$ closure coefficient, $\hat{\alpha}^* = \beta/3$
α^* damping function defined as $\alpha^* = (\hat{\alpha}^*+R_t^*/R_k)/(1+R_t^*/R_k)$
β closure coefficient, $\beta = 3/40$
β^* the damping function defined as $\beta^* = \frac{9}{100}(5/18+(R_t^*/R_\beta)^4)/(1+(R_t^*/R_\beta)^4)$
ΔV volume of computational cell [m^{-3}]
Δt time step [s]
ε turbulence dissipation [m^2 s^{-3}]
v kinematic viscosity [m^2 s^{-1}]

* Corresponding author. Tel.: 001 212 854 2956; fax: 001 212 854 3304; e-mail: modi@columbia.edu

0017–9310/98/$—see front matter
PII: S0017–9310(98)00215–4

θ temperature [K]
ρ fluid density [kg m^{-3}]
σ_ω closure coefficient, $\sigma_\omega = 1/2$
σ_k^* closure coefficient, $\sigma_k^* = 1/2$
ω specific dissipation of kinetic energy [s^{-1}].

Subscripts
o impingement
t turbulence.

Superscripts
n the time level
$+$ wall units.

1. Introduction

Fluid flows encountered in industrial electrochemical applications are frequently turbulent. One such application is through-mask electrodeposition, an important step in the manufacture of electronic, magnetic and micro-electro-mechanical (MEMS) devices. Electrodeposition is usually a wet process, other wet processes being electroless deposition, electrochemical and chemical etching, and water rinsing. Mass transport in these 'wet processes' is frequently achieved in a reactor where a single jet or an array of jets of electrolytic fluid impinges on a surface on which the deposition is to occur, e.g. a fountain plater.

A flow field created by jet impingement offers the advantages of simple design and yet an increased mass transfer rate compared to a shear flow reactor. The flow field created by impinging jets is quite complex, varying from a stagnation type flow to a wall jet type of flow with considerable curvature of streamlines. If the flow field is confined between the impingement plate and a confinement wall then recirculation regions may be present as well. Hence this particular flow configuration is considered a demanding one from the perspective of turbulence modeling alone.

Additionally the high Schmidt numbers (of the order of 1000) encountered in electrochemical systems lead to concentration boundary layers near the impingement plate that are an order of magnitude thinner than the thin wall jet boundary layers. Consequently resolution of these concentration boundary layers also pose a challenge in order to compute the mass transfer. The goal of the present study is to address the problem of prediction of mass transfer in the simplest possible system that has the combined features of impinging turbulent jets as well as high Schmidt numbers.

A jet may either issue from a slot, (usually of spanwise dimension much larger than the jet width, B) or a circular orifice. If the jet fluid is the same as the otherwise stagnant fluid into which the jet emerges then the jet is said to be submerged. The jet is said to be confined if there are other walls present in addition to the impingement surface. The impingement surface may itself be moving or stationary; and may be either flush or have roughness or discrete structures located on it. In the present study a single, confined, submerged slot jet impinging on a stationary flush surface is of interest as shown in Fig. 1. The jet Reynolds numbers, Re (based on a slot width B and the mean jet velocity v_{in}) of interest in the present study are in the turbulent flow regime. The concentration at the impingement plate or the cathode under mass transfer limited conditions is assumed constant and its normalized value is taken to be unity. The equivalent heat transfer problem corresponds to a constant temperature boundary condition.

In the present work a k–ω turbulence model by Wilcox [1] is used to compute the flow and concentration field at high Schmidt numbers for turbulent impinging jet flows. Heyerichs and Pollard [2] have successfully demonstrated that the predicted Nusselt numbers for turbulent jet heat transfer using a k–ω model have much better agreement with experimental data than those using a k–ε based solver. Temperature field calculations at $Pr = O(1)$ are also carried out in order to permit comparisons with existing experimental heat transfer data to lend additional support to the validity of the flow solver. The Sherwood numbers from the mass transfer calculations are compared with the experimental data and correlations of Alkire and Ju [3] or AJ87. The Nusselt numbers from the heat transfer calculations are compared to the experimental data of Gardon and Akfirat [4] or GA66. In addition the computed fluid velocities are compared to the experimental velocity field data of Ashforth-Frost et al. [5] or AF97.

If density variations due to concentration changes (or equivalently temperature changes for heat transfer studies) can be ignored then the problem of determining the fluid flow is uncoupled from that of determining the concentration or temperature field. The a priori determination of the turbulent flow field is of interest to those attempting to predict the heat transfer in such geometries as well. Moreover existing experimental heat transfer data can also assist in the validation of the turbulent flow. Consequently heat transfer studies in the same geometry are of interest as well even though they are likely to be in the range of Prandtl numbers O(1).

Due to their common use in industrial heat and mass transfer applications, impinging slot jets have been studied by a number of authors both numerically and experimentally. A comprehensive review of experimental work, numerical simulations and theoretical analysis of impinging liquid jets including single and multiple slot and axisymmetric jets was presented by Webb and Ma [6].

In one of the first comprehensive studies of its kind, GA66 obtained experimental heat transfer data for a single submerged, confined slot jet impinging on a flush

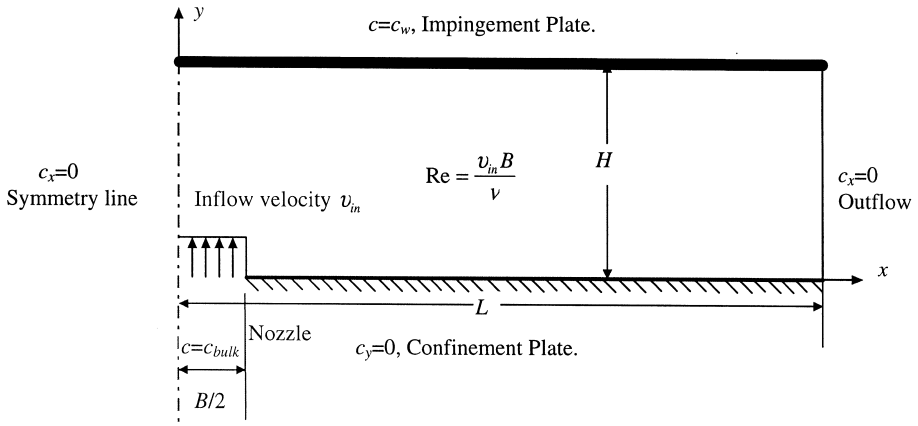

Fig. 1. Schematic of the computational domain. Computations are carried out only in the symmetric half of the domain shown.

surface. Their experiment spanned a range of jet flow speeds: from a laminar jet with $Re = 450$ up to a turbulent jet with Re in excess of 20 000 with $2 < H/B < 32$. The impingement plate was maintained at constant temperature. Polat, Mujumdar and Douglas [7] measured local and average heat transfer coefficients for a confined turbulent slot jet on a permeable surface for a wide range of Reynolds number. These studies among others provide a range of experimental heat transfer data in the turbulent regime. However due to the difficulty of making near wall velocity measurements very limited experimental fluid flow data is available for turbulent impinging slot jets.

Using laser-Doppler anemometery, Yoshida et al. [8] measured mean velocity and turbulence intensity at several locations along the impingement surface for a confined submerged impinging slot jet at $Re = 10\,000$ and $H/B = 8$. In a recent investigation, AF97 reported velocity field measurements in a semiconfined impinging slot jet geometry. The normalized distance from nozzle to impingement plate H/B was 4 or 9.2, with $Re = 20\,000$. They also measured heat transfer at $Pr = 0.7$, however a constant flux boundary condition was imposed. For small values of H/B, a secondary maximum in heat transfer was found around the point of transition to a turbulent wall jet along the impinging plate.

The previously cited experimental studies were all conducted using air with Prandtl numbers of the order of unity. At higher Prandtl numbers, recovery factor and heat transfer coefficients using transformer oil ($200 < Pr < 270$) were obtained by Ma et al. [9]. The study focused on initially laminar confined slot jets with $55 < Re < 415$ and $2 < H/B < 32$. They also report the secondary peak in Nusselt numbers ascribed to transition from a laminar to turbulent flow regime.

Mass transfer measurements for a submerged and semi-confined impinging slot jet with $Sc = 2400$ were performed by AJ87 using an electrochemical technique. The jet Reynolds number ranged from 500 to 3000, and two H/B values, 5 and 9.4 were investigated. Most of their experimental results are reported in the form of correlations and will be discussed in detail in later sections. Chin and Agarwal [10] measured the local mass transfer rates of free submerged normal and oblique impinging slot jets with an electrochemical limiting current technique. The Reynolds numbers of the experiment ranged from 1000 to 7000 and with a $Sc = 1600$. A secondary maximum in mass transfer on the impingement wall is reported at x/B between 5 and 8 for the case of normal impingement. The exact location of the hump was reported to depend on the Reynolds number, but no specific relations were given.

Besides experimental work, a number of authors performed numerical simulations in their effort to understand the fluid flow and heat transfer of slot impinging jets. Dianat et al. [11] used a k–ε and a second-moment closure model to predict turbulent fluid flow due to impingement of axisymmetric and slot jets. Comparisons of model predictions with experimental data in the stagnation and wall jet regions revealed that for the axisymmetric case, second-moment closure was superior in predicting the wall shear stress and velocity fluctuations whereas for the slot jet second-moment closure as well as the k–ε model were equally good. Heyerichs and Pollard [2] compared several two equation models for predicting impinging turbulent slot jet heat transfer. Among models considered were k–ε turbulence models with wall functions and low Reynolds number modifications of Launder and Sharma [12] and Lam and Bremhorst [13], and the k–ω model of Wilcox [1]. They found that the k–ω model provides the best prediction for heat transfer. Using the standard k–ε and RNG based k–ε turbulence models, Zhang [14] examined normal and angled impinging jets for a wide range of H/B ratios. These models however did not provide agreement with exper-

imental data that was as good as that reported by Heyerichs and Pollard [2] using the Wilcox [1] k–ω model.

2. Numerical scheme and turbulence model

2.1. Fluid flow equations

The time averaged fluid flow is solved using the Reynolds Averaged Navier–Stokes (RANS) equations with the turbulence stresses modeled using a turbulent eddy viscosity v_t. For the incompressible two-dimensional turbulent flow with constant fluid properties, the RANS equations take the following form,

$$\frac{\partial u_i}{\partial x_i} = 0, \tag{1}$$

$$\frac{Du_i}{Dt} = -\frac{1}{\rho}\frac{\partial p}{\partial x_i} + \frac{\partial}{\partial x_j}\left[(v+v_t)\left(\frac{\partial u_i}{\partial x_j}+\frac{\partial u_j}{\partial x_i}\right)\right], \tag{2}$$

where u_i is mean velocity, x_i is the coordinate, t is the time, p is the pressure, ρ is density, and v is kinematic viscosity. To solve equations (1) and (2), one needs a turbulence model to obtain v_t at each point in the flow. The Wilcox [1] k–ω model is adopted in the present study. Accordingly, the turbulent viscosity v_t is calculated as follows,

$$\frac{Dk}{Dt} = \frac{\partial}{\partial x_i}\left[(v+\sigma_k^* v_t)\frac{\partial k}{\partial x_i}\right] + G - \beta^*\omega k, \tag{3}$$

$$\frac{D\omega}{Dt} = \frac{\partial}{\partial x_i}\left[(v+\sigma_\omega v_t)\frac{\partial \omega}{\partial x_i}\right] + \alpha\frac{\omega}{k}G - \beta\omega^2, \tag{4}$$

where k is turbulent kinetic energy, ω is the specific dissipation of kinetic energy and is related to turbulence dissipation ε by:

$$\omega = \frac{\varepsilon}{k\beta^*}, \tag{5}$$

and then v_t is calculated by,

$$v_t = \alpha^*\frac{k}{\omega}. \tag{6}$$

The quantity G in equation (3), is the production rate of turbulent kinetic energy. It is defined and calculated as,

$$G = -\overline{u_i'u_j'}\frac{\partial u_i}{\partial x_j} = v_t\left(\frac{\partial u_i}{\partial x_j}+\frac{\partial u_j}{\partial x_i}\right)\frac{\partial u_i}{\partial x_j}, \tag{7}$$

where $-\overline{u_i'u_j'}$ is the turbulent Reynolds stress. The damping functions α^* in equation (6), α in equation (4), and β^* in equation (3) are calculated as:

$$\alpha^* = \frac{\hat{\alpha}^* + R_t^*/R_k}{1+R_t^*/R_k}, \tag{8}$$

$$\alpha = \frac{5}{9}\cdot\frac{\hat{\alpha}+R_t^*/R_w}{1+R_t^*/R_w}(\alpha^*)^{-1}, \tag{9}$$

$$\beta^* = \frac{9}{100}\frac{5/18+(R_t^*/R_\beta)^4}{1+(R_t^*/R_\beta)^4}, \tag{10}$$

where $R_t^*$is the turbulent Reynolds number defined as,

$$R_t^* = \frac{k}{\omega v}. \tag{11}$$

The closure coefficients are $\sigma_k^* = 1/2$, $\beta = 3/40$, $R_\beta = 8$, $R_w = 2.7$, $\sigma_\omega = 1/2$, $\hat{\alpha}^* = \beta/3$, $\hat{\alpha} = 1/10$, and $R_k = 6$. In order to obtain the mean velocity field, equations (1)–(4), and (6) must be solved to a steady state with appropriate boundary conditions.

An existing Navier–Stokes equation solver for primitive variables has been adopted to carry out the calculations. The main features of this code are a cell-centered finite volume formulation, evaluation of fluxes using a hybrid scheme, second and fourth order artificial dissipation, five-stage Runge–Kutta time stepping with local time steps and implicit residual smoothing. The details of the numerical scheme can be found in Zhang [14]. Modest second and fourth order artificial dissipation terms are used to suppress the possible high frequency oscillations. These may occur since the hybrid scheme reduces to a central difference scheme for grid Peclet numbers less than 2. The coefficients of both the second and fourth order artificial dissipation terms are set to be 0.0005, Jameson et al. [15].

In the following discretization the emphasis is on the treatment of the source terms on the right hand side of equations (3) and (4). The discretization of the other terms is the same as that of Zhang [14]. After integration over a control volume, equations (3) and (4) become,

$$\frac{\partial k}{\partial t}\Delta V = -\oint_s k u_i \,\mathrm{d}s_i + \oint_s (v+\sigma_k^* v_t)\frac{\partial k}{\partial x_i}\,\mathrm{d}s_i + G\Delta V - \beta^*\omega k\Delta V, \tag{12}$$

$$\frac{\partial \omega}{\partial t}\Delta V = -\oint_s \omega u_i \,\mathrm{d}s_i + \oint_s (v+\sigma_\omega v_t)\frac{\partial \omega}{\partial x_i}\,\mathrm{d}s_i + \alpha\frac{\omega}{k}G\Delta V - \beta\omega^2\Delta V, \tag{13}$$

where ΔV is the volume of the cell, s_i is the area of the surface in the i direction of the control volume. On the right-hand side of equations (12) and (13), k and ω at time level n, k^n and ω^n, are used in all terms on the right-hand side except the last term in each of the equations. In these negative source terms of equation (12), k at time level $n+1$, k^{n+1}, is used, and equation (12) is rewritten as:

$$\left(1+\beta^*\omega\Delta V\frac{\Delta t}{\Delta V}\right)k^{n+1} = \left(-\oint_s k^n u_i \,\mathrm{d}s_i + \oint_s (v+\sigma_k^* v_t)\frac{\partial k^n}{\partial x_i}\,\mathrm{d}s_i + G\Delta V\right)\frac{\Delta t}{\Delta V} + k^n, \tag{14}$$

where Δt is the time step. Using $\omega^n\omega^{n+1}$ to replace ω^2 in

the last term of equation (13), the equation is rewritten as:

$$\left(1+\beta\omega^n\Delta V\frac{\Delta t}{\Delta V}\right)\omega^{n+1}=\left(-\oint_s\omega^n u_i\,\mathrm{d}s_i+\oint_s(v+\sigma_\omega v_t)\frac{\partial\omega^n}{\partial x_i}\mathrm{d}s_i+\alpha\frac{\omega^n}{k}G\Delta V\right)\frac{\Delta t}{\Delta V}+\omega^n. \quad (15)$$

The discretized equations (14) and (15) are solved for k^{n+1} and ω^{n+1}, and v_t is then calculated by equation (6) to provide the closure for RANS equations (1) and (2).

In solving the fluid flow, equations (1) and (2) are solved for a given v_t in order to obtain the velocity field. Using this velocity field, equations (14), (15), and (6) are solved to provide a better estimate of v_t in order to resolve equations (1) and (2). Hence the estimate of v_t in equations (1) and (2) always lags by one time step until the steady state is obtained. Residual smoothing is not used for the k or ω equations. The time step used for the integration of k and ω equations is half of the local time step used for equations (1) and (2).

2.2. Convection diffusion equations

Assuming that the chemical species is not involved in homogeneous reactions, the material balance can be written as,

$$\frac{\partial u_i c}{\partial x_i}=\frac{\partial}{\partial x_i}\left[\left(\frac{v}{Sc}+\frac{v_t}{Sc_t}\right)\frac{\partial c}{\partial x_i}\right], \quad (16)$$

where c is the mean concentration of chemical species, Sc, the molecular Schmidt number is the ratio of the kinetic viscosity v to the diffusion coefficient D, and Sc_t is the turbulent Schmidt number. The same governing equation can also be applied to heat transfer (with no internal generation of heat and negligible viscous dissipation) with temperature field θ, Prandtl number Pr, and turbulence Prandtl number Pr_t replacing c, Sc, and Sc_t respectively in equation (16). Note that in the mean concentration (temperature) equation (16) above, the eddy diffusivity for concentration (heat) has been replaced by the ratio of the eddy diffusivity for momentum to the turbulent Schmidt (Prandtl) number. Kays [16] report a range of values for Pr_t between 0.73 and 0.92 for a molecular Prandtl number of 0.71. According to Kays and Crawford [17], the molecular Pr number has little effect on Pr_t which is close to unity in most of fluid flow, except in regions close to the wall ($y^+ < 6$). At these distances the Pr_t varies with y^+ (the dimensionless distance from the wall in wall units), but at high molecular Prandtl numbers this variation is not well understood lacking any experimental data. One option is to assume that the Pr_t variation with y^+ at high molecular Pr numbers is the same as that at molecular Pr around unity. Lacking a better alternative, this assumption is indeed made, so that one can examine whether the Pr_t (y^+) dependence has any effect on the mass transfer. A relationship suggested by Jayatillake [18] and also recently explored by Behnia et al [19]:

$$\mathrm{Pr}_t=\frac{1}{0.5882+0.228(v_t/v)-0.0441(v_t/v)^2} \quad (17)$$

is assumed. The effect of this relationship for Pr_t or Sc_t as well as constant Pr_t or Sc_t assumptions such as $Pr_t = 0.73$ and 0.90 is examined on the local Sherwood number.

In the above convection–diffusion equation the velocity field is obtained from the solution to the momentum and continuity equations. Since the Schmidt numbers of interest are of the order of 1000, the concentration boundary layer is an order of magnitude thinner than the hydrodynamic wall jet boundary layer. Consequently a much smaller grid spacing is needed to solve for the concentration than necessary to solve the fluid flow. This refinement is only needed in the direction normal to the impingement wall, as this is the direction with the dominant gradients. To avoid the additional computational expense of solving the flow as well on a fine grid, the flow is obtained on a coarser grid. The coarser flow grid solution, (velocity components u_i and turbulent viscosity v_t) is then interpolated linearly on to the finer concentration grid. A schematic of the typical concentration and flow grids near the impingement wall is shown in Fig. 2. Note that for heat transfer calculations the flow grid is also adequate in order to solve for the temperature field.

Linear interpolation ensures that the velocity field near the impingement wall follows the linear behavior of the

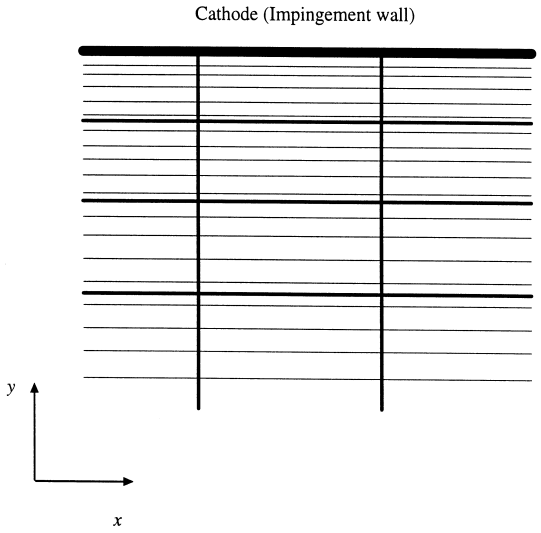

Fig. 2. Schematic of the fluid flow (dark lines) and mass transfer (light lines) grids. The x = constant grid lines are the same for both fluid flow and mass transfer.

viscous sublayer within $y^+ < 5$, the region where the concentration gradients are the largest. The adequacy of a linearly interpolated velocity field elsewhere is verified by ensuring that grid refinement of the flow field does not alter the concentration solution. It turns out that even a small error in the ability of the interpolated velocity field to satisfy the continuity equation can lead to a spurious concentration field, a problem reported in an earlier study by Yang [20]. In the present work, the interpolated velocity field is forced to be continuity satisfying by integrating the u-component of velocity to obtain a streamfunction at each vertex (of the concentration grid) along $x =$ constant grid lines. The integration process is carried out beginning from the impingement plate to preserve the accuracy of shear computation there, and ending at the confinement wall which is an insulator as shown in Fig. 1. If continuity is perfectly satisfied by the interpolated field all of these integrations along $x =$ constant lines would lead to the same value of streamfunction at the confinement wall. In the present study they differ by no more than 0.2%, a measure of the accumulated error in continuity.

Once this is done, the convection–diffusion equation is solved using an existing solver described in Chen et al. [21]. The solver used is a control volume based code, with concentration or temperature defined at cell centers and the streamfunction defined at cell vertices. The solver utilizes a power-law scheme [22] for evaluating the fluxes at the cell faces and the discretized equations are then solved using a successive over-relaxation method. Successive grid refinement is carried out to ensure that the concentration solver results are mesh independent.

2.3. Boundary conditions

A sketch of the geometry is shown in Fig. 1. Observe that due to symmetry, only the symmetric half of the domain is shown. The computational domain was truncated at $L/B = 55$ as calculations beyond this length did not alter the results in the domain of interest which was limited to x/B values always less than 40. The boundary conditions utilized in the calculations are listed below. At no slip walls the kinetic energy is set to zero but there is no obvious choice of boundary condition for the quantity ω. As recommended by Wilcox [1] at a no slip wall the boundary condition for ω is imposed at the first grid point off the wall using,

$$\omega = \frac{6\nu}{\beta y^2}, \quad y^+ < 2.5 \tag{18}$$

To use the above boundary condition it is important to ensure that the first grid point off the wall is located at a y^+ value less than 2.5. Note that in the description below u and v are the x and y components of velocity and for heat transfer calculations the concentration c is replaced by temperature θ. Both the heat and mass transfer problems of interest here have constant concentration or temperature conditions imposed at the target wall. The boundary conditions at each of the boundary segments are given below. The x and y subscripts correspond to the partial derivatives with respect to x and y.

2.3.1. Symmetry boundary

$$u_x = 0, \quad v_x = 0, \quad p_x = 0, \quad k_x = 0, \quad \omega_x = 0, \quad c_x = 0.$$

2.3.2. Impingement wall

$$u = 0, \quad v = 0, \quad k = 0, \quad c = c_w$$

The pressure on the wall is extrapolated as if the second derivative is zero. The boundary condition for ω is obtained from equation (18).

2.3.3. Outflow

Outflow conditions are specified at $L/B = 55$ (40 for laminar flow cases), a computational domain length chosen to ensure that the flow is not changing rapidly,

$$u_x = 0, \quad v_x = 0, \quad p = P_0, \quad k_x = 0, \quad \omega_x = 0, \quad c_x = 0.$$

2.3.4. Nozzle

$$u = 0, \quad v = v_{\text{in}}, \quad c = c_{\text{bulk}}.$$

Pressure is extrapolated as if the second derivative is zero. The turbulent kinetic energy at the inlet is set to be $k = \frac{3}{2}(Iv_{\text{in}})^2$, where I is the level of turbulence intensity.

2.3.5. Confinement wall

$$u = 0, \quad v = 0, \quad k = 0, \quad c_y = 0$$

The pressure at the wall is extrapolated as if the second derivative is zero. The boundary condition for ω is obtained from equation (18).

2.4. Mesh independence

To ensure that the turbulent fluid flow solutions are independent of mesh size a base case of $Re = 11\,000$ with $H/B = 5$ and $I = 4\%$ was computed for two different mesh sizes in the y direction. The two meshes had 130 and 170 non-uniformly spaced control volumes in the y direction. The stretching factor was not allowed to exceed 1.1. The distance from the first node off the wall (i.e. to the center of the first control volume) to the wall for the two meshes was $y^+ = 2.5$ and 1.5 in wall units based on the maximum shear. The number of control volumes and the control volume sizes in the x direction were not altered and maintained at 100 for both the calculations. The variation in the skin friction coefficient C_f at the impingement wall with x/B for both meshes is plotted in Fig. 3. The skin friction curves at the impingement plate for the two different mesh sizes do not show an appreciable difference. Hence in all subsequent computations the first

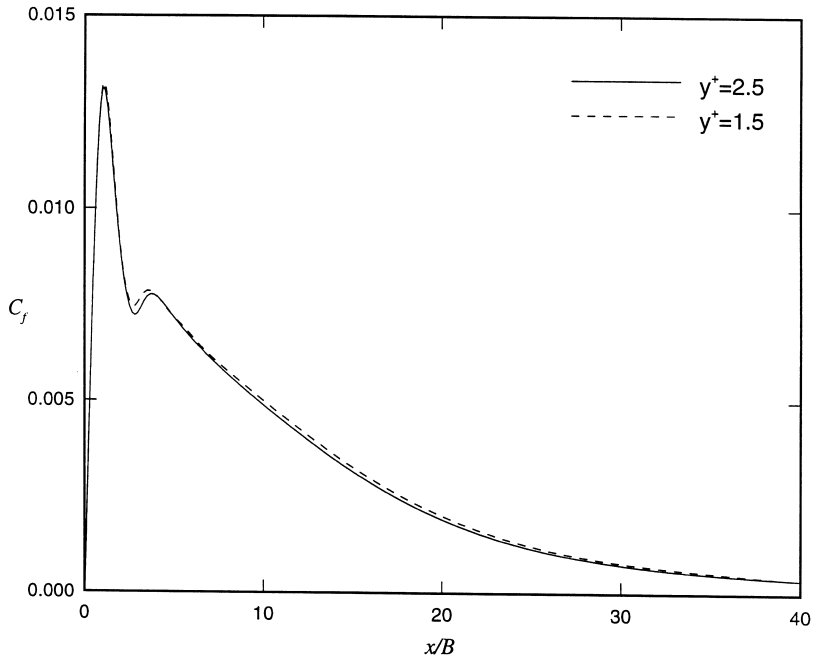

Fig. 3. Skin friction variation with x/B for two different grids. The solid line is for a grid of 100×130 and dashed line is for a grid of 100×170. The first nodes off the wall are at $y^+ = 2.5$ and $y^+ = 1.5$ respectively.

node off the impingement plate was maintained at or below a y^+ of 2.5.

A similar mesh independence study was also carried out for the mass transport solver. With a given fluid flow at $Re = 11\,000$ and $H/B = 5$, the most stringent mass transfer case expected is that for the highest Schmidt number of 2400 examined here. Sherwood numbers were computed for three successively finer grids, with the first grid point away from the wall at y^+ equal to 0.4, 0.2 and 0.1 respectively. The results of this grid refinement study shown in Fig. 4 demonstrate that it is necessary to maintain the y^+ distance of the first node off the target wall to a value no greater than 0.2 for the mass transport computation. Note that this distance is an order of magnitude lower than the nearest point for the fluid flow solver, consistent with the general trend that the concentration boundary layers are thinner by a factor of the order of $Sc^{1/3}$. All subsequent high Schmidt number mass transport calculations are performed with the first node off the wall at $y^+ < 0.2$.

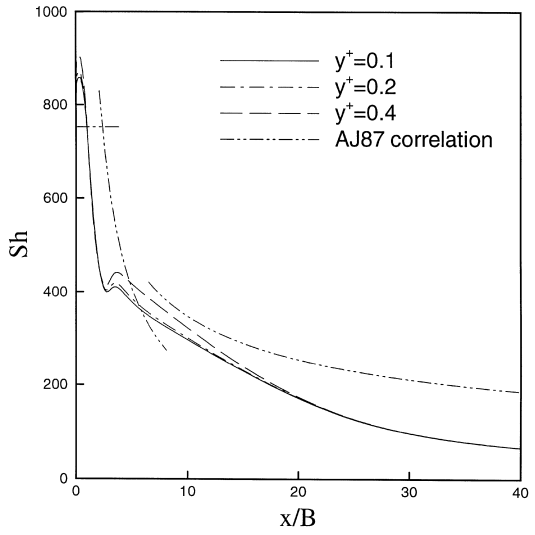

Fig. 4. Computed variation of $\overline{Sh_0}$ with x/B for three different grids with the first grid point away from the wall at $y^+ = 0.1$, 0.2 and 0.4. The AJ87 correlation is also presented.

3. Preliminary calculations

Preliminary calculations were carried out first to ascertain the ability of numerical codes to predict experimental data that were obtained without the combined complexity of turbulent flow and high Schmidt numbers. The choice of test case parameters was determined by the availability of experimental data. Even though turbulent flows are of primary interest, the solvers were first validated under laminar flow conditions with existing heat

transfer data of GA66 and mass transfer data of AJ87. Laminar flow comparisons permit the validation of the heat and mass transfer solvers without the ambiguities introduced by the turbulence model and the turbulent Prandtl or Schmidt number assumptions. The second test case was chosen to validate the flow solver under turbulent conditions with the velocity field data of AF97. The third test case was chosen to validate the heat/mass transfer solver at *Pr* or *Sc* of O(1) under turbulent flow conditions using the heat transfer data of GA66.

3.1. *Laminar flow heat/mass transfer*: Re = 450; Pr = 0.72, Re = 500 *and* Sc = 2400

For the laminar flow tests, the turbulence model equations are not solved and the turbulent eddy viscosity is set to zero, $v_t = 0$. The boundary conditions for velocity and concentration or temperature are the same as described earlier, except a parabolic velocity profile is specified at the nozzle instead of the top hat profile. Heat transfer calculations with $Pr = 0.72$ are carried out for $H/B = 4$, $Re = 450$ for comparison with the experimental results of GA66. Mass transfer calculations at $Sc = 2400$ are carried out for $H/B = 5$, $Re = 500$ for comparison with the experimental results of AJ87. A computational domain length of $L/B = 40$ is used for both cases. The heat transfer results reported here are obtained with a non-uniform mesh of 90 by 80 (80 in y direction) with the same mesh used for fluid flow. For the mass transfer calculations the fluid flow is solved on a non-uniform mesh of 90 by 80 whereas the concentration field is solved on a non-uniform mesh of 90 by 160. Tests at coarser and finer meshes were carried out to establish the mesh independence of the fluid flow, heat transfer and mass transfer calculations.

The results of both the laminar heat and mass transfer simulations are summarized in Fig. 5. The variation of the Sherwood and Nusselt numbers with x/B, the dimensionless distance along the impingement plate is shown in Fig. 5. The Nusselt and Sherwood numbers are normalized with $Pr^{1/3}$ and $Sc^{1/3}$ respectively. The experimentally obtained correlations of AJ87 for submerged laminar slot jets are:

impingement region,

$$-1 < x/B < 1, \quad Sh = 1.07 Re^{0.5} Sc^{1/3} (H/B)^{-0.20}, \tag{19}$$

transition region,

$$1 < x/B < 7.5, \quad Sh = 0.516 Re^{0.58} Sc^{1/3} (x/B)^{-0.82}, \tag{20}$$

wall jet region,

$$x/B > 7.5, \quad Sh = 0.143 Re^{0.67} Sc^{1/3} (x/B)^{-0.45}. \tag{21}$$

Observe that the scaled results for $Nu/Pr^{1/3}$ and $Sh/Sc^{1/3}$ collapse well despite the fact that the Prandtl and Schmidt numbers are several orders apart. Both *Sh* and *Nu* peak in the stagnation region, decrease rapidly in the transition region and then gradually reduce in the wall jet region.

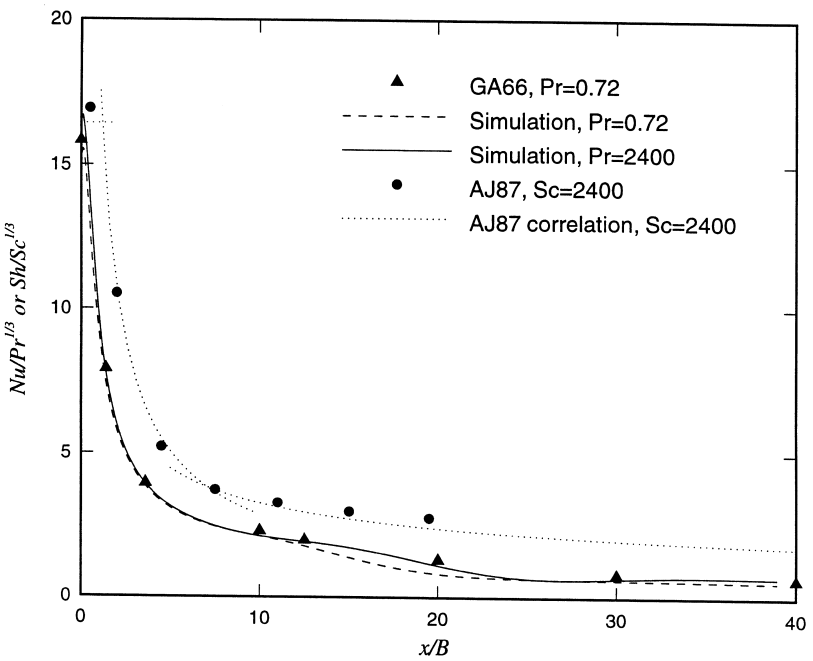

Fig. 5. Variation of computed *Sh* and *Nu* with x/B along with AJ87 correlation ($Re = 500$, $H/B = 5$, $Sc = 2400$) and GA66 data.

There is excellent agreement between the computed and experimental heat transfer results. The agreement between the computed and experimental stagnation Sherwood number Sh_0 results is not as good. In the transition and the lateral flow regions, there is reasonable agreement in the mass transfer results however the simulations generally underestimate the experimental results. The stagnation region $Sh_0/Sc^{1/3}$ are higher than $Nu_0/Pr^{1/3}$ for both the simulations and the experiments. The primary reason for this difference could be the difference in the Reynolds numbers.

3.2. *Fluid flow*: Re = 20 000

The experimental velocity field data of AF97 at $Re = 20\,000$ and $H/B = 4$ provide an excellent test case for the flow solver since their velocity measurements near the wall are at a distance close enough to the wall to permit resolution of the shear. In the experiment, a confined and submerged air jet is used. The turbulence intensity at the nozzle is maintained at 1% and the velocity profile at nozzle is flat. The variation of the normalized x-component of the mean velocities u/v_{in} with the normal distance from the impingement wall, $(H-y)/B$ is reported at several x/B positions along the impingement wall in Fig. 6(a) and (b). The present simulations show quantitative agreement with the AF97 data both in the direction normal as well as along the impingement wall except for x/B values less than 2. The differences observed in this region could be partially attributed to the fact that the mean velocities increase dramatically from $x/B = 1$ to $x/B = 2$ in the near wall region.

3.3. *Heat transfer*: Re = 11 000 *and* Pr = 0.72

The experimental heat transfer data of GA66 also encompass the turbulent flow regime of $Re = 11\,000$ with $H/B = 5$ and $I = 2.5\%$. These experiments carried out with air, $Pr = 0.72$, also provide a test case to validate the turbulent fluid flow solver. Simulations for this case were compared with the experimental data of GA66. The computed variation in Nusselt number at the impingement wall with x/B is shown in Fig. 7 along with the experimental data of GA66. The agreement is good, with a secondary peak in Sh observed in both the simulations and the experimental data although the hump is exaggerated by the simulation. In the simulations, the hump coincides with a secondary peak in kinetic energy. Based on their experimental evidence, a number of authors [4, 5, 10] ascribed the hump to the transition from laminar to turbulent boundary layers. The authors speculate that in order to simulate the secondary peak correctly, one needs to predict the location and the magnitude of the secondary peak in kinetic energy.

4. Turbulent flow mass transfer results

The primary objective of this study is the development of predictive tools for high Sc mass transfer in turbulent

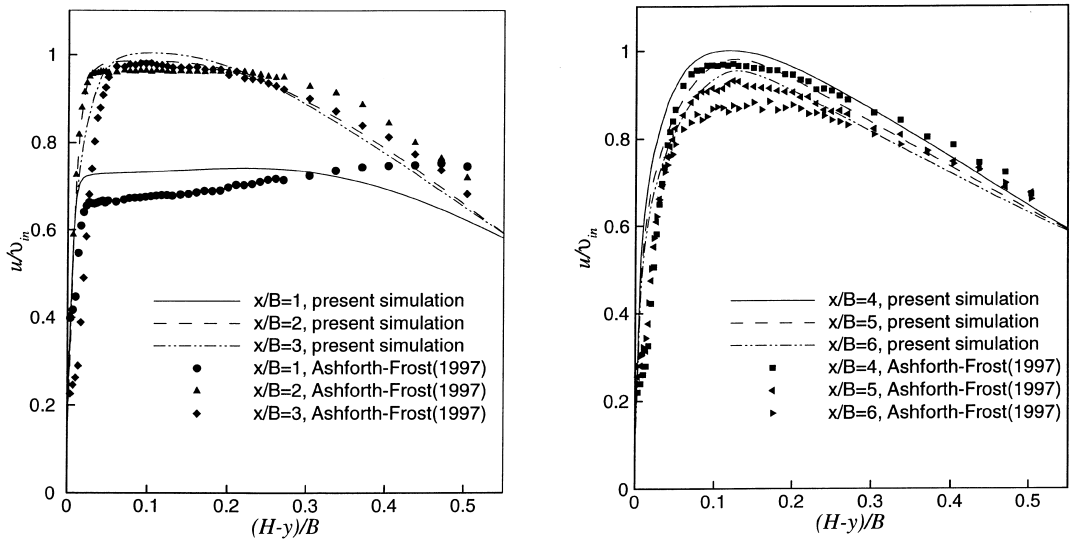

Fig. 6. Comparison of the computed x-component of the mean velocity with the experimental data of AF97 for $Re = 20\,000$ and $H/B = 4$.

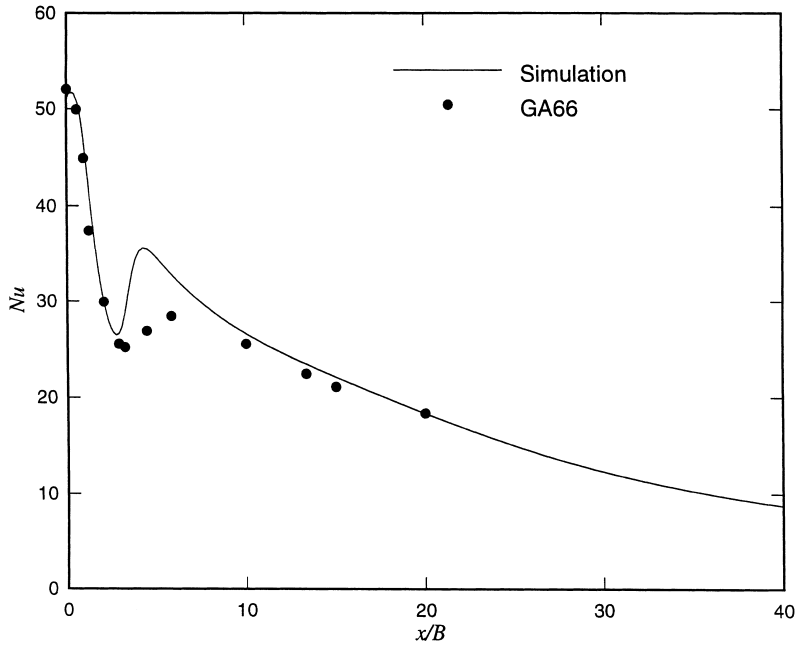

Fig. 7. Comparison of the computed and GA66 variation of Nu with x/B for $Re = 11\,000$, $Pr = 0.72$, and $H/B = 5$.

impingement flows. In this section mass transfer results are reported for the turbulent flow regime for a range of Re (from 5720 to 20 000), Sc (from 0.72 to 2400) and H/B (from 2 to 8). Where possible, experimentally obtained correlations of AJ87 are also plotted for comparison. The base case explored is for $Re = 11\,000$, $Sc = 2400$, $H/B = 5$.

4.1. *Effect of* x/b, *distance along impingement wall*

Fluid flow and mass transfer calculations for the base case are carried out with a turbulence intensity $I = 4\%$. The computed variation of Sherwood number with distance along the impingement wall is plotted in Fig. 8. Note that the secondary peak in the Sherwood number is considerably lower than the corresponding peak in the Nusselt number for the heat transfer calculations in Fig. 7. Otherwise the overall Sherwood number trend is similar to the Nusselt number trend reported in Fig. 7.

For the purpose of comparison the experimentally determined correlations of AJ87 are also plotted in Fig. 8. The correlations in AJ87 are broken down in three different regions, the impingement region, the transition region and the wall jet region. The correlations are reproduced below using the nomenclature of the present paper.

Impingement region

$$-2 < x/B < 2, \quad Sh_0 = 0.739 Re^{0.5} Sc^{1/3} (H/B)^{-0.20}, \tag{22}$$

Transition region

$$2 < x/B < 7.5, \quad Sh = 0.516 Re^{0.58} Sc^{1/3} (x/B)^{-0.82}, \tag{23}$$

Wall jet region

$$x/B > 7.5, \quad Sh = 0.143 Re^{0.67} Sc^{1/3} (x/B)^{-0.45}. \tag{24}$$

Note that the AJ87 correlation for the impingement region is based on the averaged flux in the region over $-2 < x/B < 2$ and hence no variation with x/B can be plotted from the correlation for the impingement region. Also note that at $x/B = 7.5$ the correlations for the transition and the wall jet regions are discontinuous. While the general trends show good agreement, it is clear that in the wall-jet region the agreement is poor.

The reason why the results are in good agreement in the impingement region but not in the wall-jet region may be due to placement of the confinement wall in AJ87. In AJ87 the confinement wall is not located at the jet inlet, but is at a distance of 32B from the nozzle inlet. Heat transfer studies of Obot et al. [23] and Behnia et al. [24] for axisymmetric impingement jets report that

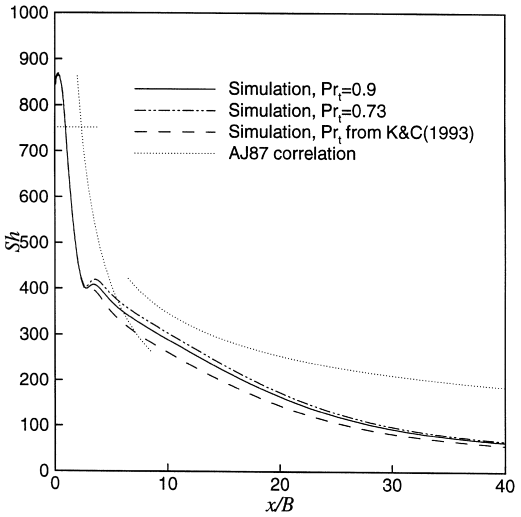

Fig. 8. Comparison of the computed Sh versus x/B variation with the correlation of AJ87 for $Re = 11\,000$, $Sc = 2400$, and $H/B = 5$. The computed results are shown for $Pr_t = 0.9$, 0.73, and Pr_t from Kays and Crawford [16].

confinement can lead to a 5–10% reduction in average heat transfer. This reduction is reported to be entirely in the region away from the impingement region. Our lower computed Nusselt numbers are qualitatively consistent with this observation. The discrepancy between the computed Sherwood number in the wall jet region and that of the AJ87 correlation grows larger with the downstream distance. Another reason for this discrepancy could be that the highest Reynolds number in the AJ87 experiments is only 3000, considerably lower than $Re = 11\,000$ where the correlation is applied here.

The mass transfer boundary layer is much thinner than the hydrodynamic boundary layer at high Schmidt numbers. In a recent study of the effect of surface roughness on the average heat transfer, Gabour and Lienhard [25] suggest that a surface can be considered smooth if the scaled roughness height is less than $12.1Re^{-0.713}Pr^{-1/3}$ or 5 microns for AJ87 experiments. While they do not report the details of the surface, most manufacturing processes would lead to surface conditions that are essentially smooth by this criterion. Hence, the authors mainly attribute the disagreement between numerical simulations and experimental data to the differences in geometry, limitations of turbulence modeling and the lower Reynolds numbers of the experiments.

The base case is also utilized for examining the effect of the turbulent Sc_t on mass transfer. The calculations at $Re = 11\,000$, $H/B = 5$, and $Sc = 2400$ are repeated for $Sc_t = 0.71$, 0.9 and equation (17) to determine the extent to which the uncertainties in turbulent Schmidt number influence the computed Sherwood numbers. As shown in Fig. 8 these three choices do not alter the computed mass transfer coefficients significantly and so a constant value of $Sc_t = 0.9$ is also used for subsequent calculations.

4.2. *Effect of* Sc

The effect of Sc variation on mass transfer is examined for the base case of $Re = 11\,000$, $H/B = 5$ and $I = 4\%$. Schmidt numbers are varied in the range of $0.72 < Sc < 2400$ and the computed Sh numbers are shown in Fig. 9. The computed Sh are shown in three different regions. The impingement region Sherwood numbers $\overline{Sh_0}$, spatially averaged over $-2 \leqslant x/B \leqslant 2$ are reported in order to facilitate comparison with the AJ87 correlations. The computed $\overline{Sh_0}$ are at most 10% lower than the AJ87 correlations. The computed dependence of $\overline{Sh_0}$ on Sc based on a least square fit works out to be $Sc^{0.342}$ while AJ97 assumes the customary $Sc^{1/3}$ dependence.

Computed results in the transition region are also shown at $x/B = 5$ and in the wall jet region are shown at $x/B = 15$ in Fig. 9. While the overall variation with Sc in these regions is similar to that in the impingement region, the computed results do show that while a customary $Sc^{1/3}$ dependence is useful for its simplicity, it may not be very accurate in the transition and the wall jet regions. The customary $Sc^{1/3}$ dependence is not captured by the present simulation in the wall jet region.

4.3. *Effect of* Re

The effect of Reynolds number variation on mass transfer is examined for the base case of $Sc = 2400$, $H/B = 5$, and $I = 4\%$ by varying Re between 5700 and 20 000. Once again the computed stagnation region $\overline{Sh_0}$ (spatially averaged over $-2 < x/B < 2$), Sh at $x/B = 5$ (in the transition region) and $x/B = 15$ (in the wall jet region) are plotted in Fig. 10. The corresponding AJ87 correlations for these parameters are also shown in Fig. 10. The computed $\overline{Sh_0}$ are at most 10% lower than the AJ87 correlation. The computed dependence of $\overline{Sh_0}$ on Re based on a least square fit works out to be very close to the $Re^{0.5}$ dependence suggested by AJ87. In the transition and wall jet regions the computations suggest a somewhat steeper Re number dependence of $Re^{0.79}$ and $Re^{0.81}$ as opposed to the $Re^{0.58}$ and $Re^{0.67}$ variations suggested by AJ87.

4.4. *Effect of* H/B

The variation of stagnation $\overline{Sh_0}$ with H/B is also examined for the base case of $Re = 11\,000$, $Sc = 2400$, and $I = 4\%$. The computed Sherwood numbers, spatially averaged in the impingement region, $\overline{Sh_0}$ in the present study are nearly independent of H/B in the H/B range of

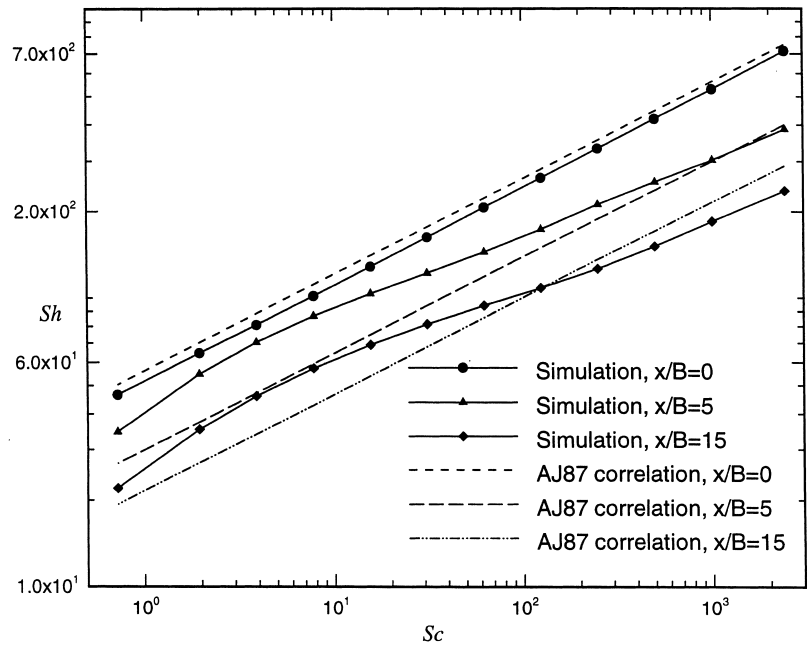

Fig. 9. Computed variation of $\overline{Sh_0}$ with Sc at $x/B = 0$, 5 and 10. The corresponding results for the three locations using AJ87 correlations are also shown.

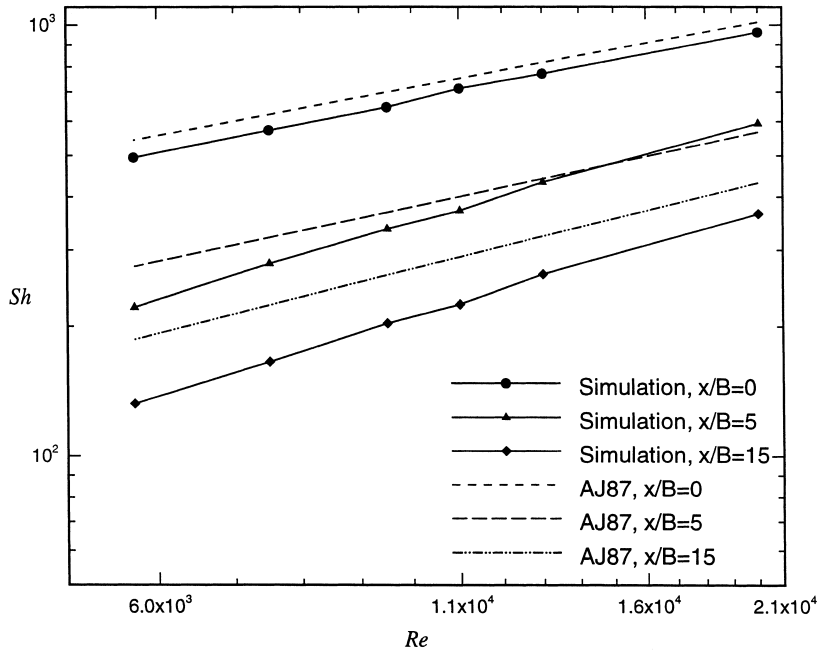

Fig. 10. Variation of $\overline{Sh_0}$ with Re at $x/B = 0$, 5 and 10. The corresponding results for the three locations using AJ87 correlations are also shown.

2–8 explored in the present study as shown in Fig. 11. The computations fail to capture $(H/B)^{-0.2}$ the variation of the AJ87 correlation at least in the small H/B range explored here. The range of values of H/B explored by AJ87 to obtain the $(H/B)^{-0.2}$ variation is not clear since actual data reported in their paper are only for a single $H/B = 5$ for the submerged jet case. Moreover, the AJ87 correlation suggests a decrease in $\overline{Sh_0}$ with an increase in H/B, a trend opposite to that suggested by the heat transfer data of GA66 where an increase in stagnation point Nusselt numbers with increase in H/B is reported for H/B less than 8.

5. Conclusions

The primary objective of this study has been to attempt to predict the mass transfer due to a submerged turbulent slot jet impinging on a smooth target wall that can be assumed to be at constant concentration. In general the predictions based on the k–ω model of Wilcox[1] agree to within about 10% with experimental data in the impingement region. While the computations capture the trends in mass transfer variations with Sc and Re, they fail to capture the dependence on H/B. This failure may be due to a combination of the weak dependence of Sh on H/B to start with and the small H/B range explored in the present study.

The study also provides some insight into computational aspects though seemingly minor, were found to be important in order to successfully compute the flow and mass transfer with the combination of high Schmidt numbers and turbulent flows.

(i) A considerably finer grid is necessary to resolve the concentration gradients than is needed to resolve the flow field. As a general rule for Sc of an order of 1000, the smallest control volumes in the concentration solver need to be an order of magnitude smaller than the smallest control volumes in the flow solver. In the range of turbulent flow Re numbers explored in this study from 5700 to 20 000, the nearest grid points were at $y^+ = 0.2$ and 2.5 respectively for the concentration and the flow solver.

(ii) It is not necessary to solve the flow field on the finer grid, instead the velocity field and the turbulent eddy diffusivity for momentum can be linearly interpolated on to the finer concentration grid. It is desirable to force the interpolated flow field to be continuity satisfying in order to avoid spurious concentration field results.

(iii) In solving the turbulence kinetic energy equation and specific dissipation of kinetic energy equations,

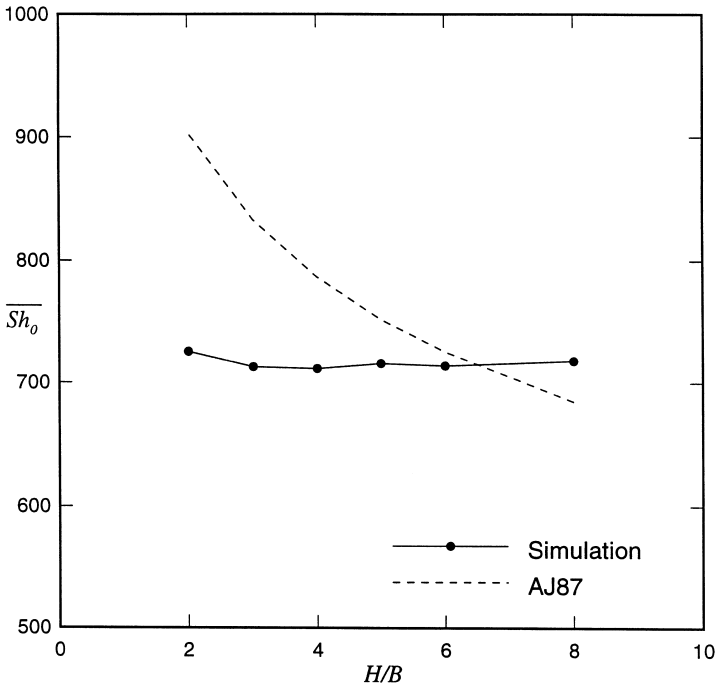

Fig. 11. Variation of the computed $\overline{Sh_0}$ with H/B. The variation suggested by the AJ87 correlation is also shown.

the negative source terms on the right-hand side need to be linearized in order to stabilize the computations scheme.

In a recent study Behnia et al. [19] used the normal-velocity relaxation turbulence model or the v^2–f model proposed by Durbin [25] to examine the heat transfer due to an axisymmetric fully developed turbulent jet. Instead of relating turbulence eddy-viscosity v_t to turbulence kinetic energy k, the v^2–f model uses v^2 which might be loosely regarded as the velocity fluctuations normal to the streamlines. The heat transfer predictions using the v^2–f model agree very well with experimental data for axisymmetric impinging jets. Future work should consider the use of this model to examine slot jet impingement as well.

The wall jet region mass transfer computations show greater disagreement with experimental data than the corresponding results for heat transfer, in the turbulent flow regime. This observation is consistent with the fact that high Sc number mass transfer is considerably more influenced by near wall behavior of turbulence than heat transfer at Pr of O(1). The near wall region is also however the weakest element in existing turbulence models. Consequently it may be necessary to employ direct numerical simulation at least in the near wall region if predictive capabilities that employ existing turbulence models are not deemed to be adequate.

Acknowledgements

This work was partially supported by the National Science Foundation under Grant CTS-93-15591 and by a TAPPI Foundation Research Award. The authors would like to thank Dr. C.-H. Sung of the David Taylor Research Center for his continued assistance with the numerical codes, Prof. Alan West for his comments and Dr. Ashforth-Frost for providing some of the experimental data.

References

[1] D.C. Wilcox, Turbulence Modeling for CFD, DCW Industries, Inc., La Canada, CA, 1994.
[2] K. Heyerichs, A. Pollard, Heat transfer in separated and impinging turbulent flows, International Journal of Heat Mass Transfer 39 (12) (1996) 2385–2400.
[3] R. Alkire, J. Ju, High speed selective electroplating with impinging two-dimensional slot jet flow, Journal of the Electrochemical Society 134 (1987) 2.
[4] R. Gardon, J.C. Akfirat, Heat transfer characteristics of impinging two-dimensional air jets, ASME Journal of Heat Transfer 101 (1966).
[5] S. Ashforth-Frost, K. Jambunathan, C.F. Whitney, Velocity and turbulence characteristics of a semiconfined orthogonally impinging slot jet, Experimental Thermal and Fluid Science 14 (1997) 60–67.
[6] B.W. Webb, C-F. Ma, Single-phase liquid jet impingement heat transfer, Advances in Heat Transfer 26 (1995) 105–217.
[7] S. Polat, A.S. Mujumdar, W.J.M. Douglas, Impingement heat transfer under a confined slot jet. Part I. Effect of surface throughflow, Canadian Journal of Chemical Engineering 69 (1) (1991) 266–273.
[8] H. Yoshida, K. Suenaga, R. Echigo, Turbulence structure and heat transfer of a two-dimensional impinging jet with gas solid suspensions, International Journal of Heat and Mass Transfer 33 (5) (1990) 859–867.
[9] C.-F. Ma, H. Zhuang, S.E. Lee, T. Gomi, Impingement heat transfer and recovery effect with submerged jets of large Prandtl number liquid—I. Unconfined circular jets, International Journal of Heat and Mass Transfer 40 (6) (1997) 1491–1500.
[10] D.-T. Chin, M. Agrawal, Mass transfer from an oblique impinging slot jet, Journal of the Electrochemical Society 138 (1991) 9.
[11] M. Dianat, M. Fairweather, W.P. Jones, Predictions of axisymmetric and two-dimensional impinging turbulent jets, International Journal of Heat and Fluid Flow 17 (1996) 530–538.
[12] B.E. Launder, B.I. Sharma, Applications of the energy-dissipation model of turbulence to the calculation of flow near a spinning disc, Lett. Heat Mass Transfer 1 (1974) 131–138.
[13] C.K.G. Lam, K.A. Bremhorst, Modified form of the k–ε model for predicting wall turbulence, Journal of Fluids Engineering 103 (1981) 456–460.
[14] J. Zhang, Numerical modeling of laminar and turbulent plane jet impingement, Ph.D thesis, Department of Applied Physics and Applied Mathematics, Columbia University, 1996.
[15] A. Jameson, W. Schmidt, E. Turkel, Numerical simulation of the Euler equations by finite volume methods using Runge–Kutta time stepping schemes, AIAA Paper, Proceedings of the AIAA Fifth Computational Fluid Dynamics Conference, 1981, pp. 1259.
[16] W.M. Kays, Turbulent Prandtl number—where are we? Journal of Heat Transfer 116, (1994) 284–295.
[17] W.M. Kays, M.E. Crawford, Convective Heat and Mass Transfer, 3rd ed., McGraw-Hill, New York, 1993.
[18] C.L. Jayatillake, The influence of Prandtl number and surface roughness on the resistance of the laminar sub-layer to momentum and heat transfer, Progress Heat and Mass Transfer 1 (1969) 193.
[19] M. Behnia, S. Parneix, P.A. Durbin, Prediction of heat transfer in a jet impinging on a flat plate, submitted to International Journal of Heat and Mass Transfer, 1997.
[20] J.D. Yang, Experimental and numerical investigation of mass transfer in electrochemical systems, Ph.D thesis, Department of Chemical Engineering, Columbia University, 1997.
[21] Q. Chen, V. Modi, A.C. West, The influence of fluid flow on leveling performance, to appear in Journal of Applied Electrochemistry 28 (1998).

[22] S.V. Patankar, Numerical heat transfer and fluid flow, Taylor and Francis, 1980.
[23] N.T. Obot, W.J.M. Douglas, A.A. Mujumdar, Effect of semi-confinement on impingement heat transfer, Proceedings of the International Heat Transfer Conference, Seventh Heat Transfer, Vol. 3, (1982) pp. 389–394.
[24] M. Behnia, S. Parneix, P. Durbin, Accurate modeling of impinging jet heat transfer, Annual Research Briefs, Center for Turbulence Research, 1997.
[25] L.A. Gabour, J.H. Lienhard, Wall roughness effects on stagnation-point heat transfer beneath an impinging liquid jet, Journal of Heat Transfer 116 (1994) 81.
[26] P. Durbin, Separated flow computations with the k–ε–$\overline{v^2}$ model, AIAA Journal 33 (4) (1995) 659–664.